Preparation and Evaluation of Siderol Amorphous Solid Dispersions: Selection of Suitable Matrix/Carrier

Maria Koromili[1,2] · Afroditi Kapourani[1] · Antigoni Koletti[3,4] · George Papandreou[1] · Andreana N. Assimopoulou[3,4] · Diamanto Lazari[2] · Panagiotis Barmpalexis[1,4]

Abstract

The present study investigates the preparation of amorphous solid dispersions (ASD) for the ent-kaurane diterpenoid siderol (SDR). Initially, evaluation of the pure drug (isolated from *Sideritis scardica*) revealed that the API is a non-stable glass former, and hence the selection of a suitable ASD's matrix/carrier needs special attention. For this reason, four commonly used polymers and copolymers, namely poly(vinylpyrrolidone), copovidone, hydroxypropyl cellulose, and Soluplus® (SOL), were screened *via* film casting and crystal growth rate measurements. Amongst them, SOL showed the highest SDR's crystal growth rate reduction, and, since it was also miscible with the drug, it was selected for further testing. In this direction, SDR-SOL ASDs were successfully prepared *via* melt-quench cooling. These formulations showed full API amorphization, while good physical stability (i.e., a stable SDR amorphous dispersions) were obtained after storage for several months. Finally, evaluation of molecular interactions (with the aid of ATR-FTIR spectroscopy) showed strong H-bonds between SOL and SDR, while the use of molecular dynamics (MD) simulations unraveled the nature of these interactions. Therefore, based on the findings of the present work, SOL seems to be an appropriate matrix/carrier for the preparation of SDR ASDs, although further studies are needed in order to explore its full potentials.

Keywords Siderol · Amorphous solid dispersions · Soluplus · Molecular dynamics simulations · Molecular interactions

✉ Panagiotis Barmpalexis
pbarmp@pharm.auth.gr

1 Laboratory of Pharmaceutical Technology, Division of Pharmaceutical Technology, School of Pharmacy, Faculty of Health Sciences, Aristotle University of Thessaloniki, 541 24 Thessaloniki, Greece

2 Laboratory of Pharmacognosy, Division of Pharmacognosy-Pharmacology, School of Pharmacy, Faculty of Health Sciences, Aristotle University of Thessaloniki, 541 24 Thessaloniki, Greece

3 Laboratory of Organic Chemistry, School of Chemical Engineering, Aristotle University of Thessaloniki, 54124 Thessaloniki, Greece

4 Center for Interdisciplinary Research and Innovation (CIRI-AUTH), Natural Products Research Centre of Excellence-AUTH (NatPro-AUTH), 57001 Thessaloniki, Greece

Introduction

Despite the development of synthetic chemistry, natural product research has sparked a lot of attention [1]. However, many of these active pharmaceutical ingredients (APIs) do not possess the necessary physiochemical and/or thermophysical properties in order to be successfully formulated into *per os* administrated pharmaceutical products [2]. SDR, which is an active ent-kaurane diterpenoid substance, is a naturally occurring compound isolated from *Sideritis* genus plants (belonging to the family of Lamiaceae) [3]. European Medicine Agency (E.M.A.) has published a full monograph on *Sideritis*, recommending its oral use (in the form of an infusion) for the treatment of mild gastrointestinal discomfort and the common cold. Moreover, several studies have shown that extracts from the aerial parts of the *Sideritis* plant demonstrate anti-inflammatory [4] and antimicrobial activity [5], while a clinical study has also proved that *Sideritis scardica* enhances the memory capacity and mood in healthy elderly people [6].

With respect to SDR, several studies have shown that the API possesses significant antimicrobial, antiviral, and anticholinesterase activities, while it is considered to have a beneficial anticancer potential [7]. In terms of its antioxidant activity, several studies have shown that SDR can be administered as a free radical scavenger against sources of oxidative stress, which is the primary cause of numerous diseases [8]. Specifically, Sagir *et al.* proved the *in vitro* antioxidant activity of SDR using three different assay methods [9]. Moreover, research regarding the ent-kaurane diterprenoids isolated from *Sideritis congesta* indicated the inhibitory activity of SDR at the superoxide anion radical scavenging activity test [10]. However, although these studies reveal that SDR can act against oxidative stress, its measured antioxidant activity is rather limited (as compared to other naturally occurring compounds). One reason for this is probably its extremely low aqueous solubility (obtained due to its ent-kaurane skeleton and its four isoprene units, see Figure S1, supplementary material), which, consequently, leads to poor oral *in vivo* bioavailability. Therefore, in order to improve SDR's antioxidant activity and enhance its oral efficacy, it is important to identify efficient formulation strategies for enhancing its aqueous solubility profile. This is especially important in the treatment of several diseases, such as periodontitis, where lower serum antioxidant levels are observed in patients, and hence the use of systematically administered antioxidants is significantly improving the therapeutic outcome [11].

In this direction, several techniques have been tested for enhancing the aqueous solubility of various naturally occurring APIs, including salt formation, particle size reduction, nano-based drug delivery systems (such as nano-emulsions, nano-lipidic formulations, etc.), and amorphous solid dispersions (ASDs) [12, 13]. ASDs appear to be one of the most successfully implemented strategies. ASDs, in general, are molecular mixtures of one or more API(s) in an inert matrix/carrier at the solid state. The matrix/carrier, which, in most cases, is a hydrophilic polymer (or copolymer), can be either a crystalline/semi-crystalline or an amorphous compound [14]. ASDs can be used to increase the dissolving rate and, in general, the solubility of poorly water-soluble drugs (PWSDs). API's solubility enhancement in this type of drug delivery system is achieved mostly due to the maintenance of the API's stable amorphization, which, in terms of thermodynamics, leads to a higher Gibbs free energy [15]. As a result, several pharmaceutical products based on ASDs have been introduced into the market, including Kaletra® (lopinavir/ritonavir), Indocin® (indomethacin), Viracept® (nelfinavir), Sporanox® (itraconazole), and Mefoxin® (cefoxitin) [16]. In the case of naturally occurring PWSD, recent attempts on ASDs include the formulation of (amongst others): (1) Baicalein (a natural active phenolic flavonoid compound extracted from the roots of *Scutellaria baicalensis*), (2) Khellin (a furanochromone class of compound and a principal constituent of *Ammi visnaga*), (3) Lutein (a xanthophyll naturally occurring carotenoids), (4) red ginseng extracts, and (5) the methanolic root powder extract of *Boerhaavia diffusa* [17–21]. In all cases, promising results were obtained, indicating that ASDs may be successfully used as an adequate drug formulation technique for improving the aqueous solubility of such nature-based PWSDs.

In this context, the present study aims to test the use of ASDs as a suitable technique for the development of an orally administered SDR formulation. As far as we can tell, this is the first enrolling attempt to evaluate the preparation of SDR-based solid oral dosage forms. For this purpose, several hydrophilic polymeric matrix/carriers, commonly used in the preparation of ASDs (such as povidone, PVP, hydroxypropyl cellulose HPC-SL, copovidone, PVP-VA, and Soluplus®, SOL), are tested/screened. The selection of these matrix/carriers was made based on their different molecular structure (see Figure S1, supplementary material) and their different physicochemical properties (see Table S1, supplementary material). The most promising system (i.e., SDR and matrix/carrier) was further tested in regard to its physicochemical–thermophysical properties and the formation of drug-matrix/carrier molecular interactions.

Material and Methods

Materials

SDR (in highly crystalline form) was derived from the hexane extract of *Sideritis scardica* (cultivated in the region of Pieria, Greece) as described in the Isolation and Identification of SDR section. PVP (Kollidon®K12), PVP-VA (Kollidon®VA64), and SOL were purchased from BASF (Ludwigshafen, Germany), while HPC-SL from Shin-Etsu (Nigata, Japan). All other reagents were of analytical or pharmaceutical grade and used as received.

Isolation and Identification of SDR

Sideritis scardica was used for the isolation of SDR. The dichloromethane and hexane extract of the aerial parts of the plant were examined in order to identify the presence of diterpenes. In brief, air-dried aerial parts of the plant (509.8 g for the first round of extraction and 1.582 kg for the second round of extraction) were finely grounded and extracted repeatedly at room temperature with 2 L of hexane and dichloromethane (three times for each solvent) for at least 48 h each time. Chromatographic methods such as CC (column chromatography), TLC (thin layer chromatography) and VLC (vacuum layer chromatography) were selected for the isolation of SDR from the initial extract. Specifically, during CC, the hexane residue of the first extraction round (~5.2 g) was subjected

to CC on silica gel 13.5×3.5 cm (Merck, Art. 9385) using hexane (He)–ethyl acetate (EtOAc) mixtures of increasing polarity as eluents to give twenty fractions (SSM-AA to SSM-AU). From these, fractions SSM-AK (eluted with He–EtOAc 80:20, 480.9 mg) and SSM-AL (eluted with He–EtOAc 75:25, 203.7 mg) were identified as SDR). For VLC, the dichloromethane residue (~6.3 g) was subjected to VLC (7.0×10.0 cm) on silica gel (Merck, Art 9385) using gradient elution with mixtures of dichloromethane (DM) and MeOH. VLC was also carried out on the He residue of the second extraction round (7.0×10.0 cm) on silica gel (Merck 60H, Art. 7736) eluted with He–EtOAc mixtures of increasing polarity. A 14.25 g of the hexane residue (20.69 g) were subjected to VLC on silica gel using He–EtOAc mixtures of increasing polarity as eluents to give seventeen fractions (SSK-AA to SSK-AR). From these, fractions SSK-AK (eluted with He–EtOAc 65:35, 1445.5 mg) and SSK-AL (eluted with He–EtOAc 60:40, 788.4 mg) were identified as SDR. TLC was used to control the quality of the fractions. For the TLC, a silica gel (Kieselgel F254, Merck, Art. 5554) stationary phase on aluminum foil (20×20 cm, 0.1 mm) with a fluorescence marker was used. The development of the TLC plates was carried out using mixtures of solvents appropriate for each group of fractions. Finally, the TLC plates were sprayed with equal volumes of 5% vanillin-H_2SO_4 solutions (Merck, Art. No. S26047 841) in MeOH and a 5% solution of concentrated H_2SO_4 in MeOH, and were heated up to 105°C for 5 min before their observation via UV/Vis spectroscopy (absorbance: 254 and 366 nm).

The identification/verification of SDR was performed *via* (1) ^{1}H NMR: Spectra were collected in an Agilent DD2 spectrometer (CA, USA). The measurements were performed at 500 MHz using CDCl$_3$ (5% *w/v* solution was used). A total of 32 scans were collected at 6 kHz sweep width. (2) Attenuated total reflection (ATR) FTIR spectroscopy: the average of sixty-four (64) successive scans (4 cm^{-1} resolution) received from 750–4000 cm^{-1} was used for obtaining SDR's spectrum. All spectra were recorded in an IR-Prestige-21-FT-IR infrared spectrometer (Shimadzu, Tokyo, Japan) connected with a horizontal MKII Golden Gate single-reflection ATR (Specac, Kent, UK) equipped with a heated diamond top plate, ZnSe lenses and a 4000 series temperature controller (heating up to 200°C). All spectra analysis was made with IRsolution *vs*. 1.30 (Shimadzu, Tokyo, Japan).

Thermophysical Characterization of SDR

Thermal Stability

Thermogravimetric analysis (TGA) was used for testing SDR's thermal stability. All measurements were conducted in a TGA-50 analyzer (Shimadzu, Tokyo, Japan). These measurements are important in order to choose whether ASD thermal processing techniques are suitable for this API. During the measurements ~5.0 mg of SDR in aluminum pans were heated from approximately 25 to 300°C under inert atmosphere (N$_2$) with a heating rate of 10°C/min. Additionally, isothermal TGA measurements were made by heating the API at for 30 min at160°C.

Glass Forming Ability (GFA)

The GFA of SDR was investigated *via* DSC based on a previously published methodology [22]. A 204 F1 Phoenix DSC (NETZSCH, Germany) was used for this study. During the measurements, ~3.0 mg of SDR were first melted at 190°C and then (after erasing its thermal history) cooled to −40°C before heating up again to 190°C. All heating/cooling processes were conducted at a heating/cooling rate of 10°C/min. Temperature and enthalpy SDs were less than 1.5°C and 3.5 J/g, respectively, in all cases. The measurements were conducted in an inert atmosphere (N$_2$). Benzophenone, indium, and tin were used to calibrate the instrument. All experiments were conducted in triplicate.

True Density Measurements

SDR density was measured in an Ultrapycnometer 1000 helium pycnometer (Quantachrome, Aston Par, Graz, Austria) by placing 100 mg of the sample previously dried at 40°C for 24 h. The measurement was conducted at 25°C and 18 psi using a flow purge for 30 min.

Selection of ASD Matrix/Carrier

The selection of the most promising matrix/carrier was performed *via* (1) film casting and (2) crystal growth rate (CGR) measurements.

Film Casting Method

During the measurements, appropriate amounts of co-dissolved SDR and each matrix/carrier (in acetone at a ratio of 50/50 *w/w*) were placed on a microscopy slide and dried under a vacuum at 45°C. All prepared films were dried to a similar extent (verified via TGA), while in all cases the drug was homogeneously dispersed (verified via high-performance liquid chromatography, HPLC). The dried films were placed under a polarized light microscope (PLM) (Olympus (BX41, Olympus Tokyo, Japan)) and API's recrystallization was evaluated via optical observation (i.e., via the birefringence). At the end of the observations with this specific methodology, the most suitable matrix/carrier was chosen.

Crystal Growth Rate (CGR)

In addition to the film-casting method, the CGRs of the amorphous SDR and the SDR-matrix/carrier ASDs were measured according to the previous methodology [23, 24]. Initially, homogeneous physical mixtures of SDR and each matrix/carrier were prepared using a mortar and a pestle (at an API/carrier ratio of 70/30 *w/w*). Then, a small amount of the sample (~ 10 mg) was placed on a microscopy slide with a cover slip and melted by heating at ~ 190°C in a Linkam THMS600 heating stage (Linkam Scientific Instruments Ltd., Surrey, UK) mounted on Olympus BX41 polarized light microscope. The melted sample was quickly cooled in order to get the ASDs. Then, SDR crystals were placed at the edge of the coverslip (used as seeds to initiate the crystallization process of the API) and the CGR of the SDR crystal interface was monitored at 80°C by taking time-lapse pictures. The CGR in all cases were determined in triplicate from the slope of the linear plot of the crystal front advancement *vs.* time.

Miscibility Evaluation

After the selection of the most suitable matrix/carrier, it is crucial to evaluate its miscibility profile with SDR in order to ensure that the prepared ASDs will be physically stable during storage. Hence, the miscibility profile of SDR in the matrix/carriers was evaluated in the below described ways:

Estimation of the Flory–Huggins (FH) Interaction Parameter

Miscibility of the ASD's components was evaluated by DSC melt depression measurements, where decreasing API's T_m and ΔH_{fus} values as the content of the matrix/carrier increases, reveals component miscibility [25]. This T_m depression is related to the FH interaction parameter (χ) based on the following Eq. (1) [26]:

$$\left(\frac{1}{T_m(1)} - \frac{1}{T_m(2)}\right) = \frac{-R}{\Delta H_{fus}}\left[ln\Phi_{(2)} + \left(1 - \frac{1}{m}\right)\Phi_{(1)} + \chi\Phi_{(1)}^2\right]$$ (1)

where $T_m(2)$ and $T_m(1)$ are the T_m of the neat SDR and the SDR in the SDR-carrier mixture, respectively; ΔH_{fus} correspond to the heat of fusion of the neat SDR, m is the ratio by volume of carrier to SDR, R is the gas constant, and $\Phi_{(2)}$ and $\Phi_{(1)}$ are SDR's and carrier's fraction by volume, respectively. The interaction parameter, χ, is estimated by the slope the of the $\Phi^2_{polymer}$ to $\left(\frac{1}{T_m(mix)} - \frac{1}{T_m(pure)}\right) * \left(\frac{\Delta H_{fus}}{-R}\right) - \left[ln\Phi_{drug} + \left(1 - \frac{1}{m}\right)\Phi_{polymer}\right]$ graphs.

Miscibility Evaluation via Solubility Parameter (δ)

SDR and matrix/carrier's miscibility was also evaluated via calculating the Hansen solubility parameters (the Hoftyzer–Van Krevelen methodology was used [27]). In this method, the total solubility parameter (δ_t) is calculated with the aid of the molar volume (V) and the dispersion (d), polar (p), and hydrogen bonding (h) forces based on the following Eq. [28]:

$$\delta_t = \sqrt{\delta_d^2 + \delta_p^2 + \delta_h^2}, \delta_d = \frac{\sum_i F_{di}}{\sum_i V_i}, \delta_p = \frac{\sqrt{\sum_i F_{pi}^2}}{\sum_i V_i}, \delta_h = \frac{\sqrt{\sum_i E_h}}{\sqrt{\sum_i V_i}}$$ (2)

Drug-carrier blends are miscible when the difference in the solubility parameters are below seven MPa$^{1/2}$ and immiscible when this difference is above ten MPa$^{1/2}$ [29].

For the determination of miscibility in respect to either temperature or concentration changes the following equation was used:

$$ln(\gamma) = \left\{\frac{V_{drug}}{RT}\right\}\left\{\left(\delta_d^{drug} - \overline{\delta}_d\right)^2 + 0.25\left[\left(\delta_p^{drug} - \overline{\delta}_p\right)^2 + \left(\delta_h^{drug} - \overline{\delta}_h\right)^2\right]\right\} + ln\left(\frac{V_{drug}}{\overline{V}}\right) + 1 - \frac{V_{drug}}{\overline{V}}$$ (3)

where γ is the activity coefficient and $\overline{\delta}$ and $\overline{V}$ are the molar volume weighted solubility parameters and the mixture volume, respectively:

$$\overline{\delta} = \sum_{k=1}^{n}\Phi_k\delta_k, \Phi_k = \frac{x_k V_k}{\overline{V}}, V_k = \frac{MW_k}{\rho_k}, \overline{V} = \sum_{k=1}^{n}x_k V_k$$ (4)

where MW and ρ are the molecular weight and density, respectively, Φ is the volume ratio, x is the molar ratio, and the k is either the drug or the matrix/carrier in the blend.

Experimental Verification of Miscibility

In addition to the above theoretical approaches, two experimental methods based on hot-stage polarized light microscopy (HSM) and DSC was used for evaluating SDR-matrix/carrier miscibility. In the case of HSM, samples of SDR with the selected matrix/carrier at a ratio of 20:80 *w/w* were heated up to 190°C on a Linkam THMS600 heating stage (Linkam Scientific Instruments Ltd, Surrey, UK) mounted on a PLM and the miscibility of the components was evaluated by visually observing the melted and the subsequently cooled mixtures. In the case of DSC, the T_g was determined from the 2nd heating scan of the samples following the organology and measuring conditions described in "Glass Forming Ability" (GFA) section.

Construction of Thermodynamic Phase Transition Diagram

A typical thermodynamic phase diagram shows the stability (transition) zones of a binary ASD system. In the present study, the phase diagram of SDR with the most promising

matrix/carrier was constructed by using the FH lattice-based solution theory given in Eq. 1 and DSC melt depression method. For solving the equation, the FH interaction parameter (χ) was assumed to be dependent on temperature:

$$\chi = A + \frac{B}{T} \tag{5}$$

where *A* and *B* are the temperature-independent and dependent terms, respectively (i.e., representing the entropic and enthalpic contribution in the mixing of the system, respectively).

Spinodal curve was constructed by plotting the 2nd derivative of the Eq. 1 when set to 0:

$$\Delta G = RT\left[\Phi_{drug}ln\Phi_{drug} + \left(\frac{1 - \Phi_{drug}}{m}\right)\ln\left(1 - \Phi_{drug}\right) + \chi\Phi_{drug}(1 - \Phi_{drug})\right] \tag{6}$$

The Gordon–Taylor (G-T) equation was used to fit the experimentally determined T_g values:

$$T_g = (w_1 Tg_1 + kw_2 Tg_2)/(w_1 + kw_2) \tag{7}$$

$$k = (\rho_1 Tg_1)/(\rho_2 Tg_2) \tag{8}$$

where w_i is the by-weight fractions of SDR and the matrix/carrier, *k* is a constant (representing a semi-quantitative measure of the interaction strength between the functional groups), and ρ are the experimentally determined densities (using the same methodology and procedure described in "True Density Measurements" section) of amorphous SDR (1.208 ± 0.053 g/cm^3) and SOL (1.082 ± 0.032 g/cm^3).

Preparation of SDR-Based ASDs

The preparation of amorphous SDR and ASDs (using the most suitable matrix/carrier) was conducted *via* the method of melt/quench-cooling. Briefly, 1.0 g in a total of the neat SDR and the selected matrix/carrier were mixed at several weight ratios (i.e., 10/90, 20/80, and 30/70 *w/w* drug to matrix/carrier) and heated to 190°C under an inert atmosphere (N_2) in order to reduce the risk of oxidative degradation. The resultant samples were quench-cooled in a freezer and the ASDs were grounded gently *via* a mortar and a pestle. The obtained ASDs were then sieved and a fraction between 100 and 150 μm was used for further analysis. The final ASDs were hermetically sealed in amber glass vials using aluminum crimp caps and placed in desiccators before further use.

Evaluation of SDR-Based ASDs

Molecular Interactions

Interactions on the molecular level between SDR and the selected matrix/carrier were evaluated *via* ATR-FTIR spectroscopy. Specifically, both the physical mixtures of the API-matrix/carrier and their ASD as well as the pure components were studied. For every spectrum, sixty-four (64) successive scans were received using the same organology and measuring parameters as once described in the "Isolation and Identification of SDR" section.

Physical State

Powder X-ray diffraction (pXRD) was used for evaluating the amorphous (or crystalline) state of SDR within the ASD samples. Specifically, a small quantity of each sample (~20–30 mg) was gently pulverized and mounted on a 28-position sample plate before measurement. All samples were analyzed using transmission pXRD on a Bruker D8 PHASER CRD-diffractometer (Bruker, MA, USA) having CuKα radiation for crystalline phase identification ($\lambda = 0.15405$ nm). Data were collected in the range $5 - 45°$ 2θ with a 0.02° 2θ step size and 0.5 s per step count time. The accuracy of the instrument was tested against a corundum A26-B29-S reference sample.

High Performance Liquid Chromatography (HPLC)

SDR's content in the prepared ASDs was estimated *via* a previously validated HPLC method [30]. The HPLC system consisted of a Shimadzu (Shimadzu, Kyoto, Japan) pump, autosampler, and ultraviolet–visible detector (codes: LC-10 AD VP, SIL-20A HT, and SPD-10A VP, respectively). The analysis was performed isocratically using acetonitrile (ACN) and water in a ratio of 70:30 *v/v* in an Agilent Eclipse XDB-C18 (150 mm, 4.6 mm, and 5 μm) column. The flow rate in the system was set at 1.0 mL/min and the samples were injected with a volume of 30 μL. SDR was detected at 240 nm. Prior to the analysis, the mobile phase was degassed for 30 min and sonicated for 15 min. Linearity for SDR was performed in the range of 5–2000.0 μg/mL ($R^2 \geq 0.999$).

Molecular Dynamics (MD) Simulations

Setting up the Initial Structures

SOL's molecular chain structure was constructed with the aid of XenoView v.3.7.9.0 (http://www.vemmer.org/xenoview/xenoview.html) based on previously published reports [31, 32]. The molecular structure of SDR was obtained from a previously published work [33]. All initial assemblies were subjected to energy minimization under the pcff_d force field. Out of the 10 minimized structures, the one with the lowest energy was used in the following steps.

Amorphous Cell Building

The amorphous cell structures for SDR (30 molecules) and SRD-SOL (10/90 *w/w*) conformations at 25°C were

constructed by varying the rotatable torsions using the free rotation model method in Xenoview. The obtained assemblies were then equilibrated by using a previously validated multi-step equilibration protocol [34].

Validation of SDR and SDR-SOL Amorphous Simulation Assemblies

SDR's and SDR-SOL molecular amorphous simulation boxes were validated *via* the following method: initially, the assemblies were equilibrated for 4.0 ns at 500 K and 1 atm. During this equilibration phase, ten Å were used as a cut-off radius and one Å as spline distance. Berendsen thermostat was used with variable volume and shape options. The equilibration was performed under periodic boundary conditions. The resultant assemblies were then subjected to MD cooling MD down to 200 K with a twenty K cooling step. A 500 ps NPT MD dynamics run was performed—the half for equilibration and the rest for data collection—and the T_g of SDR and the SDR-SOL mixtures was estimated by plotting the specific volume values (ν) against T. In the case of the neat SOL, a similar validation procedure was conducted in our previous paper [31].

Execution of MD Simulations

The molecular structures were subjected to 5.0 ns NPT MD simulation at 25°C and 1.0 atm following the Van Gunsteren and Mark validation criteria [35]. The radial distribution function (RDF, or $g(r)$) was calculated using the final two ns of the MD trajectory according to the following equation:

$$g(r) = \frac{\langle V\Sigma_{i \neq j}\delta(r - |r_{Ai} - r_{Bi}|)\rangle}{(N_A N_B - N_{AB})4\pi r^2 dr} \tag{9}$$

where A and B are specific atoms, V is the system volume, N_A and N_B are particle number of atoms A and B, respectively, N_{AB} is the number of particles belonging to atom A and atom B simultaneously, and r_{Ai} and r_{Bj} are the position of particle i of atom A particle j of atom B, respectively.

Statistical Analysis

Results are expressed as mean ± standard deviation (SD) from three replicates for each experiment. Tukey's test was used to compare the differences among various groups, and a value of $p < 0.05$ was statistically significant. All data were analyzed by using IBM SPSS Statistics software v.27 (IBM, Armonk, NY, USA).

Results and Discussion

Isolation and Identification of SDR

In order to verify that the followed extraction method was suitable in order to isolate the SDR compound from the *Sideritis scardica*, the obtained purified extract was analyzed *via* ^{1}H-NMR and FTIR spectroscopy, and the findings were compared to previously published results.

Figure 1a shows the ^{1}H-NMR spectra of the obtained compound. Results revealed several characteristic peaks at: 5.25 ppm (1H, s, H-15), 4.69 ppm (1H, t, $J = 5.0$ Hz, H-7), 3.32 ppm (1H, d, $J = 10.8$ Hz, H-18b), 3.00 ppm (1H, d, $J = 10.8$ Hz, H-18a), 2.37–2.32 ppm (1H, m, H-13), 2.06 ppm (3H, s, OAc), 1.70 ppm (3H, s, Me-17), 1.07 ppm (3H, s, Me-20), and 0.70 ppm (3H, s, Me-19). Additionally, all recorded peaks from the ^{1}H-NMR spectra of the API are depicted in Table S2 (given in supplementary material). All these ^{1}H-NMR peaks (not only the main peaks described above) were in perfect agreement with previously published NMR results for SDR [33], indicating that the isolated compound is indeed SDR.

In addition to NMR, the isolated compound was analyzed via ATR-FTIR spectroscopy (Fig. 1b). Results showed several characteristic FITR peaks recorded at 3468 cm^{-1} (due to O–H symmetrical stretching), 2928 cm^{-1} (due to C–H stretching), 1705 cm^{-1} (due to C=O symmetrical stretch), 1439 cm^{-1} (due to O=C–CH$_3$ wagging), 1382 cm^{-1} (due to C–H wagging), 1265 cm^{-1} (due to C–O symmetrical stretch) and 1056, 1043, and 1030 cm^{-1} (due to C–H rocking). All ATR-FTIR peaks recorded for SDR are depicted in Table S2 (supplementary material). As in the case of ^{1}H-NMR, all recorded FTIR peaks were in perfect agreement with SDR's FTIR spectrum published in previous studies [33].

Hence, based on the above ^{1}H-NMR and ATR-FTIR analyses, it can be said that the extraction method was able to successfully isolate the ent-kaurane diterpenoid SDR substance (with a purity of 97.0%) from the *Sideritis scardica*.

Thermal and Physicochemical Characterization of SDR

GFA of SDR

GFA is an indicator of API's ease of vitrification process [22]. Figure 2a summarizes the obtained DSC thermograms for the determination of SDR's GFA. Results in the 1st heating showed a single melting endotherm for the API (T_m at 144.9°C with a ΔH_f of 55.53 J/g). Upon reheating, a T_g was recorded at 13.7 °C, followed by a recrystallization peak (T_c at 66.1 °C and ΔH_c of 37.72 J/g) and a subsequent

**Fig. 1** ^{1}H-NMR (**a**) and ATR-FTIR (**b**) spectra of the isolated SDR
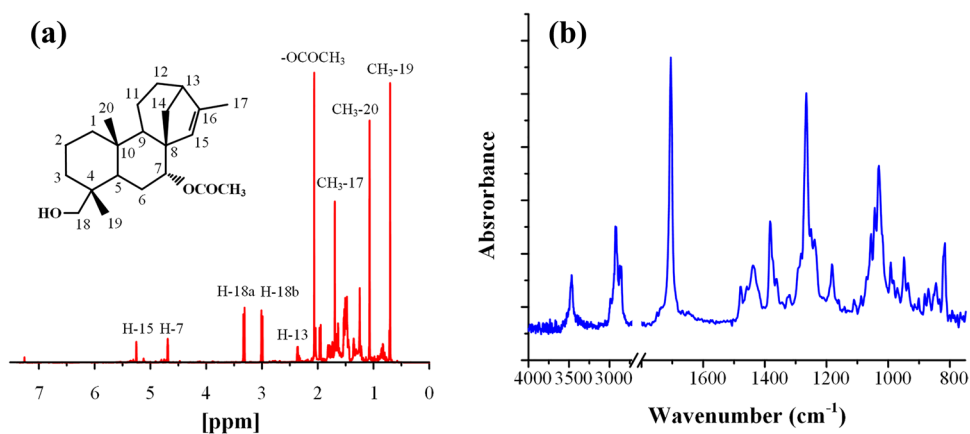
melting peak (T_m at 142.4 °C with a ΔH_f of 42.17 J/g). Hence, based on the obtained results, only a portion of SDR recrystallizes upon reheating. However, the API is considered to be a non-stable glass former (GFA Class II compound) since recrystallization (although partial) is observed upon DSC reheating. Therefore, for the preparation of a stable SDR ASD formulation the appropriate matrix/carrier(s) should be carefully selected.

Thermal Stability of SDR

In a further step, and before proceeding with the selection of the most suitable ASDs' matrix/carrier(s), it is important to investigate the thermal stability of the API. This is crucial in order to evaluate whether heat-based manufacturing processes are suitable for the preparation of SDR-based ASDs. In the present study, the thermal stability of SDR was evaluated *via* TGA. According to the obtained thermogram (presented in Fig. 2b), SDR is thermally stable up to approximately 200°C. No traces of moisture or remaining quantities of solvents (used during the extraction process) were recorded (a mass loss of less than 1% *w/w* was observed up to 200°C). Further heating of the API (i.e., above 200°C) resulted in a sharp reduction of its weight, due to rapid thermal degradation. In addition, isothermal TGA was also performed, with results (presented in Fig. 2c)

Fig. 2 **a** DSC thermograms of SDR during the heating (1st run, black)—cooling (red)—heating (2nd run, blue) cycle for the determination of GFA, **b** TGA, and **c** isothermal (at 160 °C) TGA weight loss of SDR (thermal degradation)
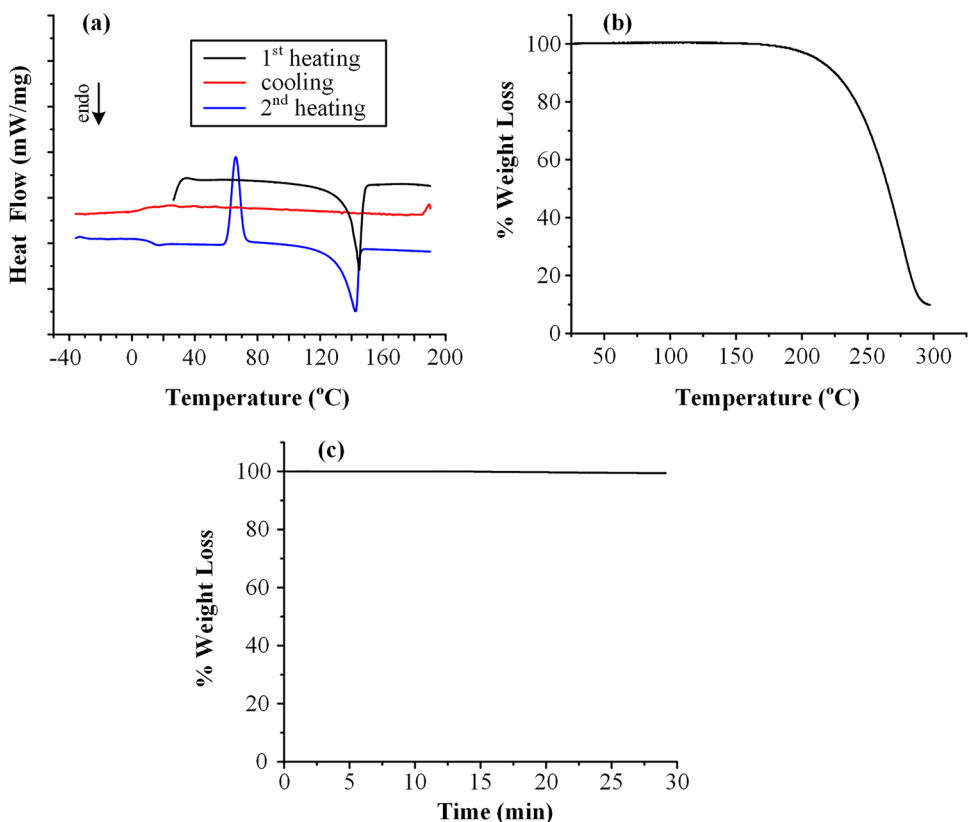
showing that the API was stable at 160°C for up to 30 min. Hence, based on these results, it is safe to conclude that the API is thermally stable up to ~200°C and that heating temperatures above its melting point (i.e., 160°C) can be safely used for ASDs manufacturing (such as melt mixing, used in the present study).

Selection of SDR's ASD Matrix/Carrier

After the evaluation of SDR's thermal and physicochemical properties, several commonly used polymers (and copolymers) were screened in order to find the most suitable ASD matrix/carrier(s). In order to do so, two distinct methods were employed.

Film-Casting Method

During the film-casting method, the evaluation of matrix/carriers is made from the visual inspection of binary ASD films (formed between the API and each matrix/carrier separately) immediately after preparation and after storage for several days in high temperature and humidity conditions. The polymer/copolymer, which achieves the most significant retardation in API's recrystallization is selected as the most suitable matrix/carrier for the preparation of ASDs.

Figure 3 summarizes the PLM images collected from the pure SDR and the binary SDR-matrix/carrier ASD films. SDR, when examined alone (i.e., without the addition of any matrix/carrier), showed quick and extended recrystallization starting almost immediately after the formation of the film (i.e., from day 1). These findings verify that the API is a GFA class II glass compound, i.e., a non-stable GF. Looking now at the binary drug-polymer films for PVP and PVP-VA, results showed high drug recrystallization, starting from day 1. This recrystallization was similar to the pure API, indicating that both tested excipients were not able to inhibit SDR's crystal growth. However, when HPC-SL was tested as a matrix/carrier, it seems that the drug's recrystallization was restricted to a large extent, at least until the 7th day of storage. Nevertheless, despite the initial promising results, a high drug recrystallization was observed on the 21st day. Conversely, SOL was the only tested matrix/carrier that succeeded in retarding the recrystallization of the API significantly until the 3rd week of the experiment, where only small crystals were evident for the first time. Hence, based on the obtained results, SOL seems to be the optimum matrix/carrier that can significantly stabilize the amorphous API during storage. It is, however, important to note that the storage conditions selected during the film-casting evaluation (all samples were stored in open vials at 40 ± 2°C/75 ± 5% RH) were chosen in order to induce any API re-crystallization and have a fast screening for the most suitable matrix/carrier. During the finished drug product formulation development

(i.e., late-stage development), additional factors, such as other excipients working as humidity protectants or the use of suitable containers (such as aluminum blisters), may significantly improve the stability of the binary SDR-SOL ASD system.

SDR's Crystal Growth Rate

In addition to the film-casting method, for the selection of the most promising ASD's matrix/carrier SDR's crystal growth rate was evaluated at 80°C. This high temperature was selected in order to accelerate the crystal growth of the API and hence, expedite the matrix/carrier selection process. Figure S2 (supplementary material) shows the PLM images collected from the conducted experiments. Results clearly showed that, compared to the binary drug-matrix/carrier ASDs, the pure API possesses higher crystal growth rates. Specifically, pure SDR's crystal growth rate at 80°C was estimated at 0.94 ± 0.05 mm/s, whereas the binary ASDs showed rates of 0.08 ± 0.01, 0.38 ± 0.02, 0.25 ± 0.05, and 0.05 ± 0.01 mm/s for PVP, HPC-SL, PVP-VA, and SOL, respectively. Hence, in all cases, the addition of the polymeric matrix/carrier resulted in a significant reduction of the drug's CGR, with SOL showing the most promising inhibition results.

Based on the above results, it seems that in some cases the two different methods used for the selection of the most suitable matrix/carrier (i.e., film-casting and CGR) do not show the same trends in recrystallization inhibition. Specifically, with film-casting PVP is one of the least favorable carriers, while with CGR PVP shows very low rates, which are comparable to SOL. Keeping in mind that the CGR measurements were conducted at 80°C and that this temperature is higher than the T_g of the SDR-PVP ASD (see Figure S3a in supplementary material), it seems that the formation of molecular interactions between the drug and PVP are favored at 80°C, leading to drug's slow crystal growth rates. This hypothesis is verified by ATR-FTIR measurements conducted for the SDR-PVP ASD at 25 and 80°C (Figure S3b, supplementary material), where a significant shift in PVP's C=O FTIR peak is recorded only at 80°C, corresponding probably to the formation of strong H-bonds between SDR's –OH and PVP's C=O groups. However, this shift (and hence H-bonds) was not recorded in the 25°C spectra of the same ASD. On the contrary, when SOL was tested as a matrix/carrier a shift in the –C(O)N stretching vibration at 1625 cm^{-1} is recorded at both 25 and 80°C (also in Figure S3b of the supplementary material) indicating that significant molecular interactions between the drug and the copolymer are being formed in both temperatures. Hence, it can be said that the reason why SOL, contrary to PVP, seems to inhibit SDR's recrystallization in both film-casting and CGR experiments is probably the formation of stronger molecular interactions between the drug and the copolymer.
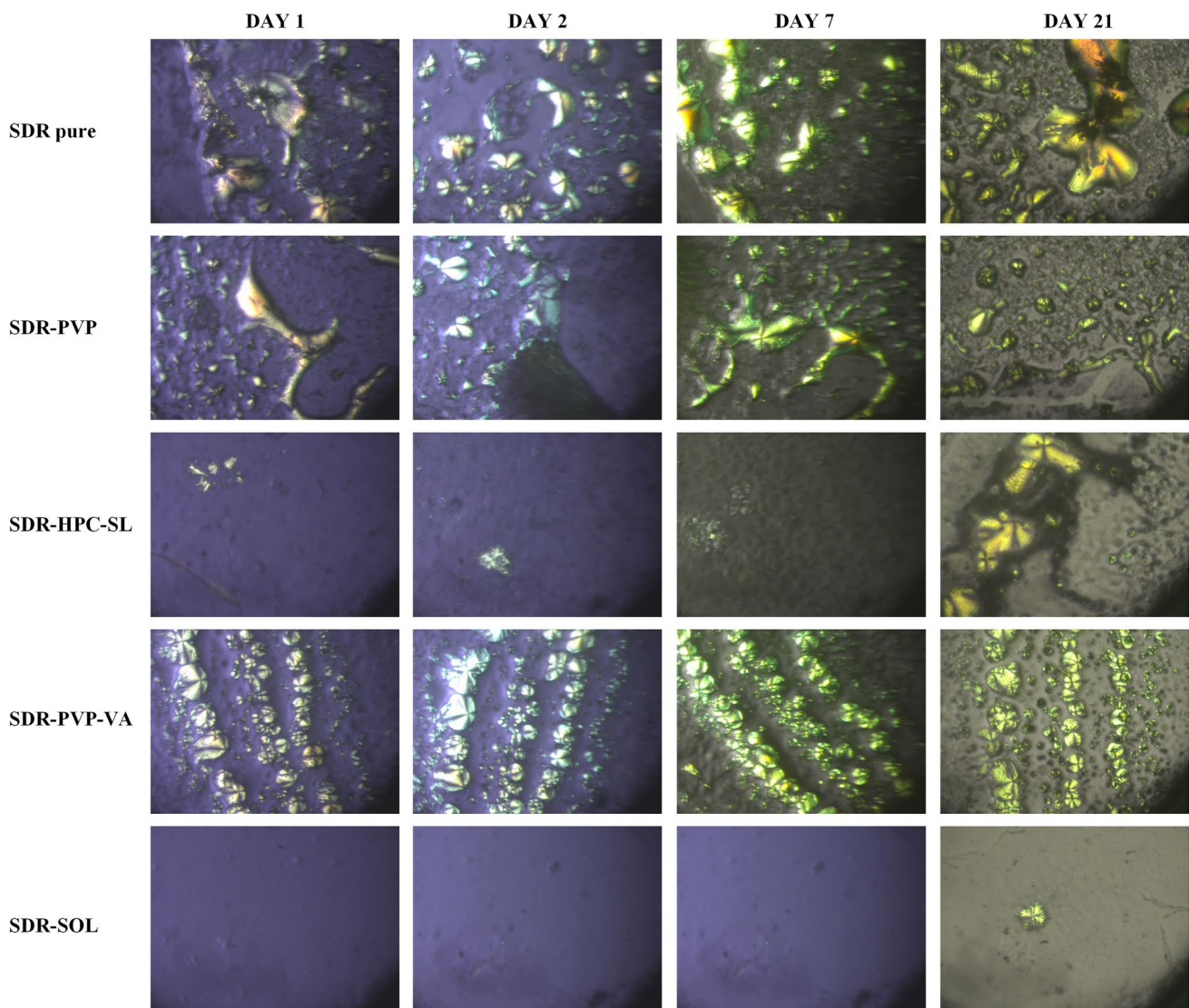
Fig. 3 PLM photographs for the selection of SDR's most suitable ASD matrix/carrier based on the film-casting method (all samples were stored in open vials at $40 \pm 2°C$ / $75 \pm 5\%$ RH)

Thus, based on both screening approaches (i.e., film-casting and crystal growth measurements) and the above analysis, it seems that SOL is the most promising matrix/carrier, and therefore, it was selected for the preparation of SDR-SOL ASDs.

SDR-SOL Miscibility Evaluation

As far as the physical stability of an ASD system is concerned, the components' miscibility is regarded as a factor of crucial importance, affecting the recrystallization tendency of the API. Should immiscibility and mutual incompatibility between the components appear, phase separation is thermodynamically favored [36].

FH-Interaction Parameter Based on DSC Melting Point Depression

Initially, the estimation of the Flory–Huggins (FH) interaction parameter took place in order to determine the components' miscibility. Figure 4a presents the plot of Φ^2_{pol} to $\left(\frac{1}{T_m(mix)} - \frac{1}{T_m(pure)}\right) * \left(\frac{\Delta H_{fus}}{-R}\right) - \ln\Phi_{SDR} - \left(1 - \frac{1}{m}\right)\Phi_{pol}$ at low polymer (i.e., SOL) concentrations, where the χ can be considered T and Φ independent. The value of the FH-interaction parameter, χ, which, according to FH lattice theory, is calculated from the slope of the presented regression line, was equal to -0.9851 ($R^2 = 0.964$). The resultant negative value of χ is indicative of a thermodynamically miscible system. Furthermore, a negative ΔG_{mix} is expected regardless of the

polymer's content, based on the decrease in SDR's melting point with increasing matrix-carrier content and the negative χ (Fig. 4b), implying overall good thermodynamic miscibility of the drug with the tested copolymer.

Hansen Solubility Parameters

Additionally, SDR-SOL miscibility was evaluated using Hansen solubility parameters. Table S3 presents the calculated Hansen solubility parameters for SDR and SOL. The number average of the three monomers was calculated to establish the solubility parameter for SOL, which is constituted of polyvinyl caprolactam (PVC): polyvinyl acetate (PVA): polyethylene glycol (PEG) in a ratio of 57:30:13. According to the obtained results, the total solubility parameter (δ_t) for SOL is equal to 21.75 MPa$^{1/2}$, while the respective parameter's value for SDR is equal to 24.94 MPa$^{1/2}$. Consequently, the absolute difference between the APIs and the polymer's solubility parameters is 3.19 MPa$^{1/2}$,

indicating that SDR and SOL, at least according to the estimated Hansen's solubility parameters are miscible. This finding agrees with the thermodynamic miscibility evaluation according to the FH interaction parameter χ.

In a further step, the temperature-related miscibility of the two components was evaluated theoretically based on the activity coefficient (γ) using the previously calculated Hansen's solubility parameters. Figure 4c shows the activity coefficient of SDR *vs.* temperature for different weight fractions of SDR to SOL along with the ideal mixing line (i.e., $\ln\gamma = 0$). When $\ln\gamma < 0$ components may be considered miscible. According to the obtained results, as temperature increases, the $\ln\gamma$ curves cross the ideal mixing line, indicating a correlation between temperature and SDR – SOL miscibility. Similarly, the obtained graphs show that as the API content increases, the activity coefficient curves shift to lower $\ln\gamma$(SDR) values, indicating a strong correlation between components' miscibility and API's content, with increasing miscibility obtained in higher SDR to SOL weight ratios.
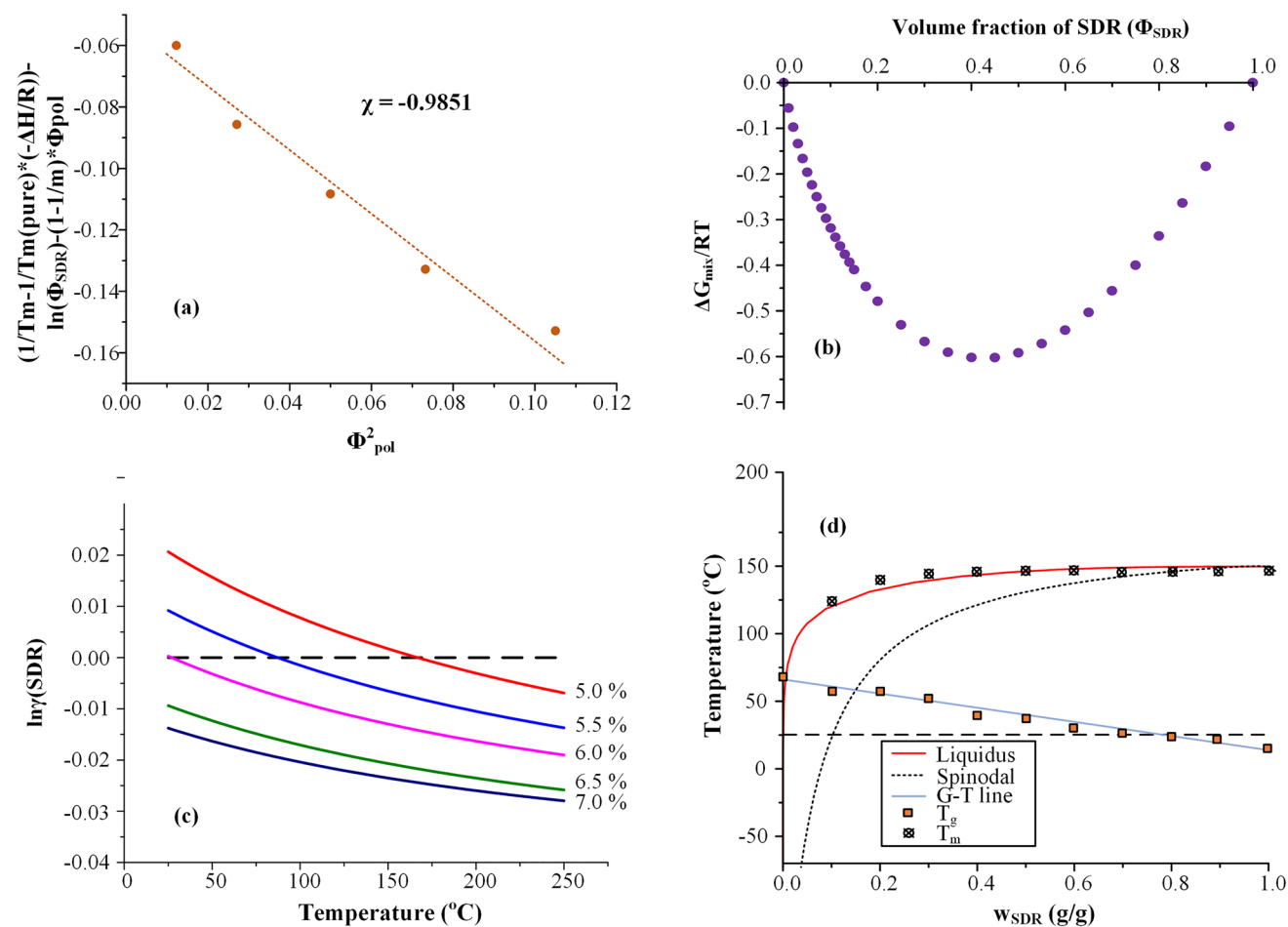

Fig. 4 **a** FH interaction parameter estimation plot; **b** $\Delta G_{mix}/RT$ *vs* Φ_{SDR} plot (b); **c** activity coefficient (γ) *vs* temperature plot (percentages correspond to the weight fraction of SDR to SOL and the horizontal dashed line represents the ideal mixing line, i.e.,

$\ln_\gamma$(SDR) = 0); **d** thermodynamic phase transition diagram of SDR-SOL based on FH lattice theory. Black dashed line represents the 25°C (commonly selected storage temperature for solid oral dosage forms)

Experimental Verification of Miscibility via HSM

In addition to the above theoretical approaches, the miscibility of the two compounds was evaluated experimentally. Although there are several techniques used for the evaluation of components' miscibility, such as pXRD, solid-state NMR [37, 38], in the present study HSM and DSC were used, since the former is a cost-effective method where miscibility in the melt state can be easily detected through optical observations (a miscible mixture forms a uniform liquid melt), while the latter is a common and easy to implement method where the presence of a single T_g indicates the miscibility of the two components. According to the pictures and the DSC thermograms recorded in Figure S4 (supplementary material), SDR and SOL were completely miscible both in the melt state and also after cooling, as there were no distinct melting/separation zones formed between the two components, and only one T_g was recorded in the DSC thermograms. These findings verify the previous theoretically derived results (based on FH interaction parameter and Hansen solubility parameters) and prove that both approaches can reliably predict the miscibility of the two components.

SDR-SOL Phase Diagram

In a further step, after establishing that the two components are miscible within each other during the melting process (and hence, the possibilities of developing a stable ASD system for SDR using SOL are highly increasing), it is important to evaluate the solubility and phase transition behavior of the system (i.e., determine the physical state changes induced in respect to temperature and composition) before proceeding with the preparation and evaluation of the ASD systems.

For this reason, the temperature-composition phase diagram based on FH theory were constructed. These diagrams provide a framework according to which the performance of the SDR within the polymeric matrix is getting understood in respect to changes in composition and temperature. Characteristically, the phase diagram predicts the maximum solubility of the drug and the miscibility of amorphous drug in the examined carrier as a function of both temperature and composition. Specifically, the liquidus curve (i.e., solubility curve) illustrates the fraction of the API (crystalline or amorphous) dissolving into the matrix/carrier, while the spinodal curve defines the boundaries between two distinct zones; the one appearing on the right-hand-side of the spinodal, where, thermodynamics-wise, is characterized as "unstable" since phase separation is favored and, the second, appearing on the left-hand-side of the spinodal until liquidus, within which the drug is present in a metastable zone, where a prevention of API's recrystallization process may take place due to the presence of the polymeric matrix/carrier.

In the present study, SDR-SOL phase diagrams were constructed using DSC melting point depression data. Figure S5 (supplementary material) shows the obtained DSC thermograms for the binary SDR-SOL mixtures during DSC 1st and 2nd heating scans, while Table S4 (supplementary material) summarizes all recorded thermal events. In order to construct the respective phase diagram, the SDR T_m (endpoint) values recorded in the 1st heating scans and the T_g values recorded in the 2nd heating scans were used. These data were fitted to Eq. 5, 6, 7, and 8, following the methodology described in the Construction of Thermodynamic Phase Transition Diagram section, in order to predict the phase transition boundaries according to FH and G-T theories. Based on Eq. 5 fitting results, the entropic (A) and enthalpic (B) constants were − 9.42 and 4188 K, respectively. Good correlation coefficient values ($R^2 > 0.95$) were obtained from the fitting of Eq. 6 to SDR's T_m data, indicating that the FH theory may adequately predict API's solubility transition within the SOL matrix/carrier (Fig. 4d). Similarly, good fitting results were also obtained for the T_g line, indicating that the G-T equation may also adequately describe the glass-rubbery changes in the investigated mixtures.

Based on the obtained phase transition results shown in Fig. 4d, it seems that the selected temperature for the preparation of the ASDs (i.e., 160°C) can fully solubilize SDR within the selected SOL matrix/carrier in all drug-to-polymer weight ratios. In addition, at 25°C (the temperature at which most drugs are stored), the suggested metastable zone is extended up to approximately 10% w/w SDR to SOL. Nevertheless, it is important to note that these boundaries are based on FH lattice theory and that in practice (along with kinetic events), parameters that are not included in the assumptions made in FH theory (such as strong intermolecular interactions) may significantly alter these set boundary limits. Nevertheless, the use of such theoretical predictions seems to be a good starting point for ASD's preliminary pre-formulation studies [39].

Preparation and Evaluation of SDR-SOL ASDs

After selecting SOL as the most promising matrix/carrier, in terms of re-crystallization inhibition, and ensuring that SDR (which is a thermally stable compound at least up to 200 °C) is completely miscible with SOL and fully solubilized in all SDR/SOL weight ratios at 160°C, ASDs of the two compounds were prepared by the melt-quench cooling approach. In all cases, (i.e., ASDs at weight ratios of 10/90, 20/80, and 30/70 w/w of SDR to SOL), glassy and highly brittle solids were prepared and analyzed in terms of physical state and molecular interactions.
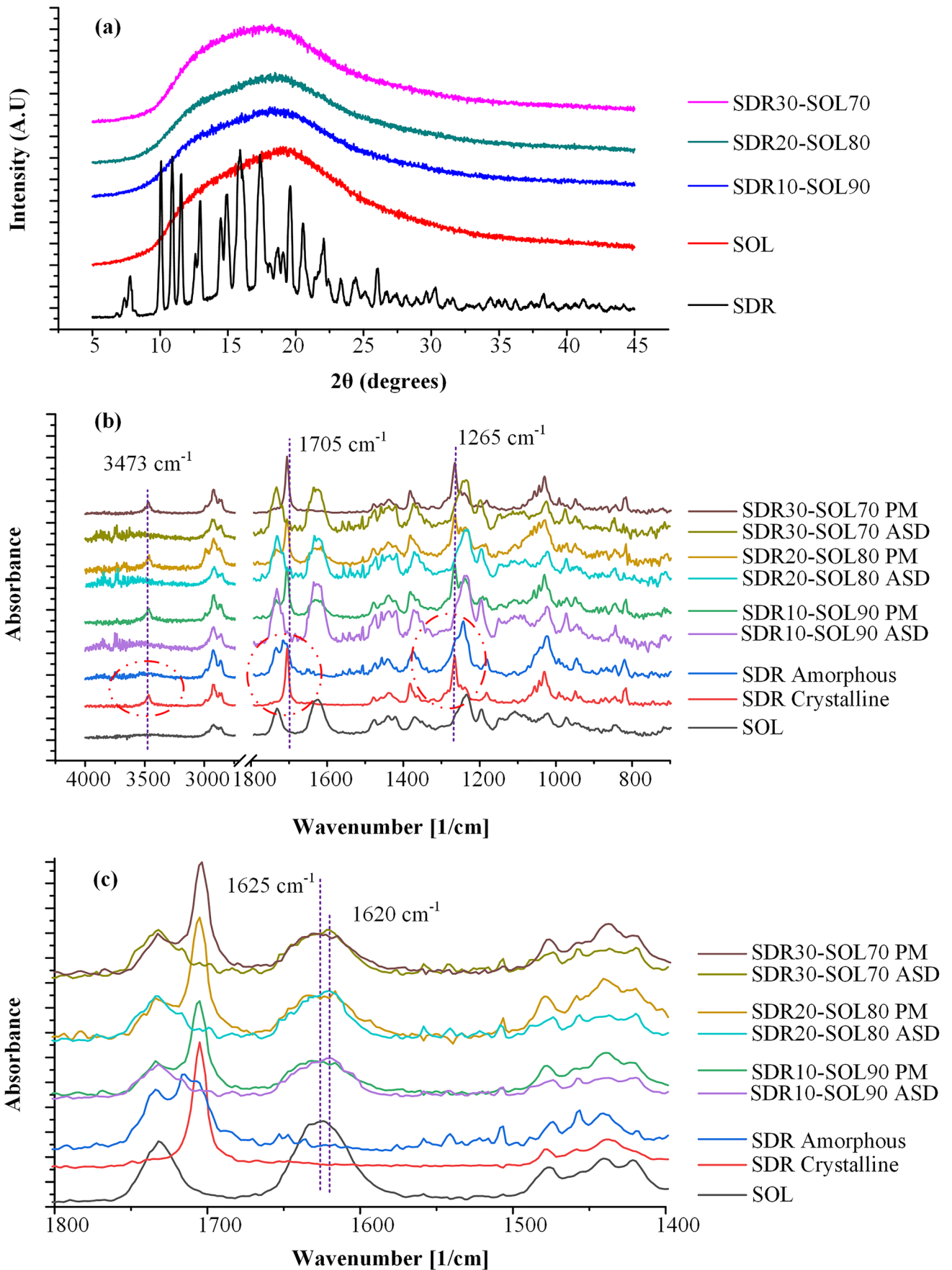
◄**Fig. 5** pXRD diffractograms of raw materials (SRD and SOL) and the prepared ASDs at several weight ratios after 2 months of storage (**a**); their ATR-FTIR spectra (along with the binary physical mixtures (PM) in 4000–750 cm^{-1} (**b**); 1800–1400 cm^{-1} (**c**) region, respectively

Physical State Evaluation

The amorphous or crystalline nature of SDR within the prepared ASDs was evaluated via pXRD was used. Figure 5a shows the recorded diffractograms for the pure SDR and pure SOL as well as the respective ASDs after 4 months of storage in closed HPDE vials at 40°C/75%RH. To the best of our knowledge, this is the first time that the pXRD diffractogram of SDR is presented, and we are the first to report that the drug is a crystalline compound with several characteristic 2θ peaks at 7.30, 7.81, 10.12, 10.89, 11.48, 12.85, 14.47, 14.90, 15.84,17.46, 18.57, 19.77, 20.45, 22.07, and 26.08°. However, it is important to note that it is not clear whether this pattern represents a single crystalline phase of SDR, or a mixture of different crystalline forms is present. In the case of SOL, the copolymer displayed an amorphous halo located in the 2θ region of 5 − 45°, indicative of its amorphous state. Regarding the prepared ASD systems, an amorphous halo was recorded in all examined cases. This indicates that SDR ASDs were successfully prepared in all weight ratios of SOL, while all studied ASDs remained amorphous during storage (amorphous halos were also recorded immediately after preparation, data not shown). Therefore, based on the obtained results, it is obvious that the implemented melt-quench cooling approach was able to prepare solid dispersion systems with fully amorphized SRD that were stable during storage.

Molecular Interactions

It is proven that the molecular interactions significantly affect the production and performance (both in terms of physical stability and bioavailability) of any ASD system. In this context, the ATR-FTIR spectra of SDR-SOL ASDs were evaluated in order to explain any kind of molecular interaction occurring between the matrix/carrier and the API.

Figure 5b shows the ATR-FTIR spectra of the initial raw materials (SOL and the crystalline SDR), the neat amorphous SDR (prepared by melt-quench cooling), and the physical mixtures (PMs) of SDR-SOL (at several weight ratios) and the respective ASD. In regard to SDR, the ATR-FTIR spectrum of the crystalline compound, which was analyzed in detail previously (see "Isolation and Identification of SDR" section during the verification/identification of the active compound), showed several characteristic absorptions peaks, with the most distinct being at 3468 cm^{-1} (due to OH symmetrical stretching), 1705 cm^{-1} (due to C=O symmetrical stretch), and 1265 cm^{-1} (due to C–O symmetrical

stretch). Inspecting now the ATR-FTIR spectra of the amorphous SDR, the API showed three significant changes (as compared to its crystalline counterpart): (a) the peak of OH stretching (at 3468 cm^{-1}) was significantly reduced (almost disappeared), (b) the peak corresponding to the C=O (at 1705 cm^{-1}) was sifted to higher wavenumber (1715 cm^{-1}) while a new (second) peak at 1733 cm^{-1} was recorded, and (c) the peak corresponding to C–O symmetrical stretching (at 1265 cm^{-1}) was shifted to lower wavenumbers (i.e., at 1241 cm^{-1}). All these changes clearly indicate that during SDR's amorphization strong molecular interactions, probably in the form of hydrogen bonds (H-bonds) between the hydroxyl hydrogens and the ketone/ester oxygens of the compound, are being formed. These interactions will be thoroughly evaluated via MD simulations in the following section.

In regard to the neat matrix/carrier (i.e., SOL) the recorded ATR-FTIR spectrum revealed several characteristic vibrational peaks with the most profound located at 2913 cm^{-1}, (corresponding to the stretching of –C-H bond), 1732 cm^{-1} (corresponding to the ester –C=O stretching) and 1625 cm^{-1} (corresponding to –C(O)N stretching).

Looking now at the obtained SDR-SOL ATR-FTIR spectra, several noticeable differences between the PMs and their respective ASDs were observed. Specifically, in the case of all PMs, the collected spectra were the sum of the individual crystalline SDR and the respective polymeric matrix/carrier (i.e., SOL). These findings suggest that no chemical interactions (between the API and the polymer) or any API amorphization occurred during the physical mixing of components. This was expected since the PM process usually does not induce any physical state changes or any molecular interactions. In contrast, the ATR-FTIR spectra of the respective ASDs showed significant differences compared to their PMs counterparts. For example, the peaks corresponding to the C=O and C–O vibrations of the API (located 1705 and 1265 cm^{-1}, respectively) were both shifted to higher and lower wavenumbers, respectively. Additionally, the peak corresponding to the OH stretching vibration of the crystalline SRD (located at 3468 cm^{-1} and recorded in all PMs) was now significantly reduced (almost eliminated) in all SDR-SOL ASDs. These observations indicate that new molecular interactions are being formed during the preparation of the ASDs. However, it is important to note that most of these API spectrum changes were also recorded in the spectrum of the neat amorphous SDR. Hence, there is a chance that the shifts recorded in the ASD's spectra are due to the formation of SDR-SDR intramolecular bonds, created within the API's amorphous structure and not due to the formation of intermolecular interactions between the API and the matrix/carrier. In the former case, i.e., the creation of drug-drug intramolecular interactions, separate drug/polymer amorphous/amorphous zones are formed, leading

to drug re-crystallization and hence, to physical instability during storage.

Therefore, in order to evaluate for intra- and inter-molecular interactions, the ASDs' spectra were closely investigated in the region of 1800–1400 cm^{-1}, i.e., the region where the –C=O and –C(O)N stretching vibrations of the neat SOL are being recorded. Looking at the obtained results (presented in Fig. 5c), it is obvious that a small shift (by ~ 5 cm^{-1}) in the –C(O)N stretching vibrations of SOL (initially recorded at 1625 cm^{-1}) is recorded in all prepared SDR-SOL ASD spectra (as compared to the respective PMs). This shift indicates that SOL's caprolactam oxygens are most probably participating in the formation of intermolecular H-bonds with SDR's hydrogen bond acceptors (e.g., OH). In addition, slight shifts in SOL's –C=O vibrational peaks (initially recorded at 1705 cm^{-1}) were also recorded in the aforementioned ASDs' spectra, however, since the C=O peaks of the amorphous API are also recorded in the same region, it is hard to say whether these changes are due to SOL participation in intermolecular interactions with the API or due to SDR's amorphization. It is crucial to note, however, that the aforementioned changes are hard to distinguish due to a high obtained signal to noise ratio. Therefore, it is unclear whether the changes in the obtained ATR-FTIR spectra are indeed due to the formation of new molecular interactions or due to the presence of the neat amorphous API. Therefore, in order to gain an insight into the suggested SDR-SOL molecular interactions, MD simulations were performed.

MD Simulations

In contrary to most experimental-based techniques (such as Raman and FTIR spectroscopy), where the extensive analysis of molecular interactions is rather difficult, computational techniques can offer comprehensive atomic-level and energetic information that can greatly aid the understanding of such interactions. Hence, based on the above ATR-FTIR analysis, where both intra- and inter- molecular interactions were identified, an attempt is now made *via* MD simulations to evaluate and unravel their true nature and extent.

Construction of Initial Molecular Structures The initial molecular structures for SDR, its neat amorphous assembly (containing 30 molecules), and SOL (along with its amorphous MD simulation structure) are shown in Figure S6 (supplementary material). Figure 6 shows the SDR-SOL amorphous assemblies before (on the left) and after (on the right) the equilibration protocol. Results clearly showed that the followed equilibration steps resulted in final amorphous structures that were much more homogeneous as compared to the initially constructed.

Validation of the MD Simulation Boxes In a further step, and before proceeding with the MD simulations, it is important to ensure that the developed MD simulation assemblies are valid and that they are reliable. In the case of SOL, the used amorphous assembly was validated previously [31], while the validation of the SRD and the SDR-SOL amorphous assemblies are presented in Figure S7 (supplementary material), where the T_g estimated values for the drug and the SDR-SOL mixtures based on the performed MD simulations, were in a close agreement with the experimentally derived values (*via* DSC). Specifically, in the case of the neat SDR, a T_g value of 295.3 K was estimated based on MD simulations which were in close agreement with the 286.8 K obtained by DSC. Similarly, for SDR-SOL amorphous mixtures, the T_g values based on the MD simulation were 337.1, 335.8, and 333.7 K, for SDR-SOL 10/90, 20/80, and 30/70 *w/w* respectively, as compared to 329.0, 325.5, and 323.9 K obtained from DSC. It is important to note that the slightly greater T_g values estimated by MD simulations were expected due to: (1) the time-dependent nature of the glass transition phenomenon (MD simulations are performed in ns timescales) and (2) the adopted significantly faster cooling rates in MD simulations, leading to early vitrification and consequently to higher T_g values (as compared to DSC experiments). However, despite these small differences, the close agreement in the simulated and experimentally determined T_g values, indicates that the selected MD parameters and constructed amorphous assembly are reliable for predicting the performance of the amorphous API and the amorphous SDR-SOL mixtures.

Intermolecular Interactions Evaluation Initially, before proceeding with the analysis of the SDR-SOL amorphous assemblies, it is important to understand the molecular interactions (and especially intermolecular H-bonds) occurring within the neat amorphous API structure. Only then, and only by evaluating the true nature of molecular interactions within the neat drug amorphous structure, we will be able to fully unravel the type and extent of the molecular interactions occurring between the drug and the matrix/carrier within the formed ASD.

For the evaluation of H-bonds in the present study, the maximum hydrogen-acceptor distance and minimum donor-hydrogen-acceptor angle were set at 2.5 Å and 90°, respectively. Based on these criteria, representative H-bond patterns for amorphous SDR are depicted in Fig. 7, where several H-bonds are depicted, especially between API's hydroxyl proton (H1, for notation, see Figure S6 supplementary material) and the ester C=O oxygens (O5). Also, in the case of SDR-SOL, several intermolecular H-bonds are being formed (Fig. 7), especially between the hydroxyl proton of SDR and the carbonyl and ether oxygens (O1 and

Fig. 6 MD simulation boxes
for SDR (green color) and SOL
(orange color) mixtures, before
(left side) and after (right side)
the adopted multistep equilibra-
tion protocol
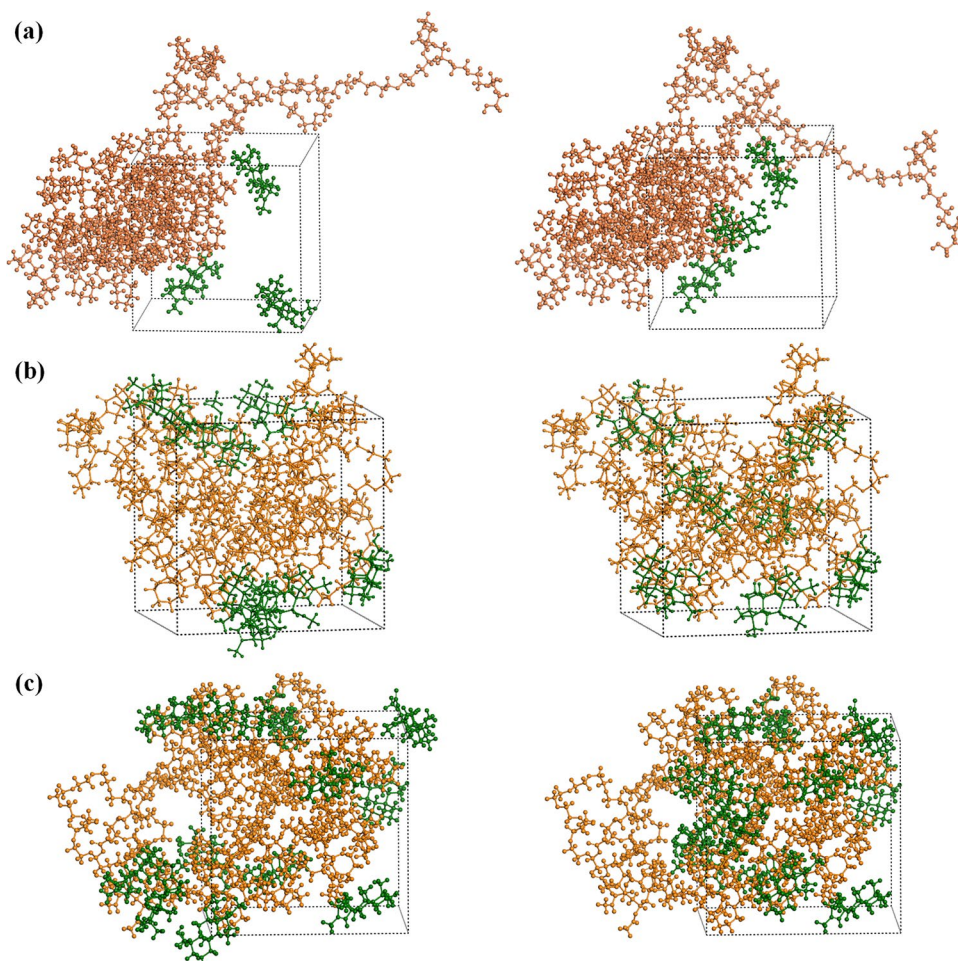
O3) of the polyvinyl caprolactam and the polyethylene gly-
col monomers for SOL.

In order to fully evaluated for these molecular interac-
tions, the $g(r)$ of several H-bond acceptors and donors (from
both API and matrix/carrier) was evaluated (Fig. 8). Before
moving with the analysis of the results, it is important to note
that in such $g(r)$ graphs, donor–acceptor distances below
2.5 Å indicate strong molecular interactions between the
involved atoms, while distances from 2.5 to 3.2 Å and 3.2 to
4.0 Å indicate moderate and weak interactions, respectively.

Regarding amorphous SDR, Fig. 8a shows one strong
$g(r)$ peak for H1… O5 (located at 1.84 Å), indicating the
formation of strong intermolecular H-bonds between the
hydroxyl proton (H1) and the ester (C=O) oxygen of SDR.
These interactions may provide a good explanation of the
OH and C=O vibration peak changes recorded for the amor-
phous API ATR-FTIR spectrum (see Molecular Interactions
section).

With respect to SDR-SOL ASDs, results in Fig. 8b, c, and
d shows that the formation of intermolecular interactions
depends on the weight content of the API. Specifically, in

ASDs having low API content, that is 10% *w/w*, results in
Fig. 8b show the formation of three low-intensity $g(r)$ peaks
located at ~2.0–2.1 Å. All these peaks were between the H1
proton of the API and the main H-bond acceptor oxygens of
the matrix/carrier (i.e., the polyvinyl caprolactam's C=O
(O1), the polyvinyl acetate's C=O (O2) and the polyethyl-
ene glycol ester oxygen (O3)), while no significant interac-
tions were recorded between the API itself. On the contrary,
when the content of the API's increases to 20% *w/w*, two
strong $g(r)$ peaks are recorded (Fig. 8c) attributed to the for-
mation of intermolecular interactions between the OH proton
of the API (H1) and the ester oxygen (O5) of SDR and poly-
vinyl caprolactam's C=O (O1) of SOL. Further increase
of API's content to 30% *w/w* results in the strengthening of
the intermolecular interactions between SDR's amorphous
molecules (Fig. 8d). Hence, based on the obtained results,
it seems that at low API concentrations (10% *w/w*), SDR's
molecules form H-bonds only with SOL, leading thus to the
formation of a molecularly dispersed ASD system. On the
contrary, increasing API's content increases the probabil-
ity of SDR's molecules interacting with each other in the

Fig. 7 H-bonds in amorphous SIM (**a**) and SDR-SOL (**b**) assemblies (H-bonds are depicted with blue dashed lines)
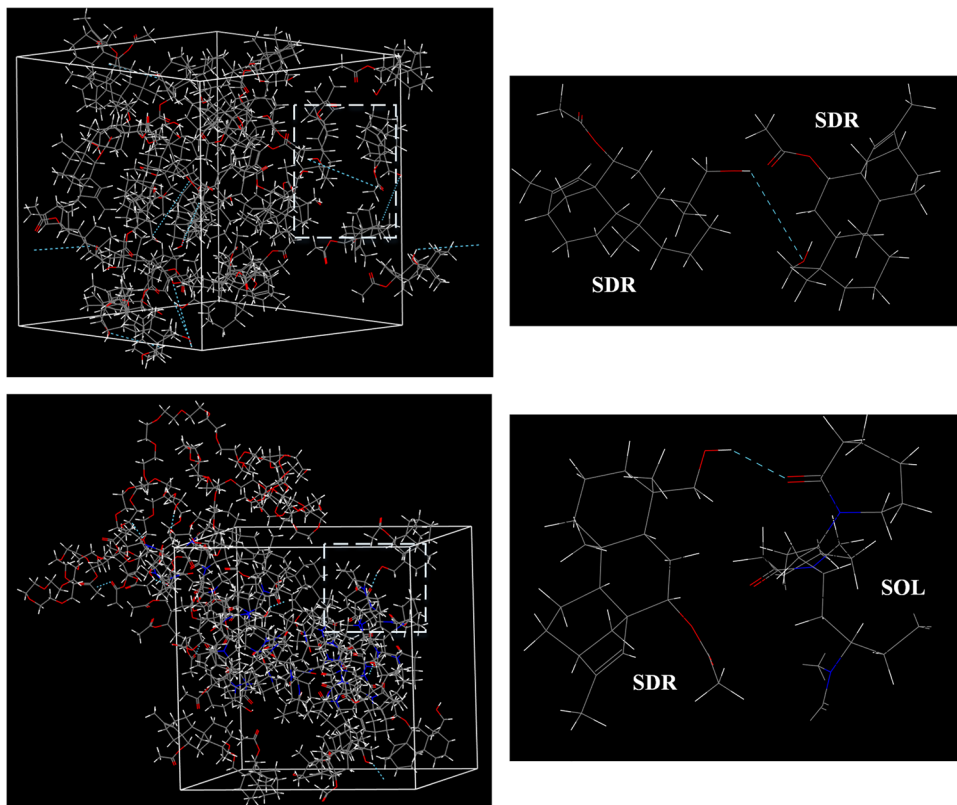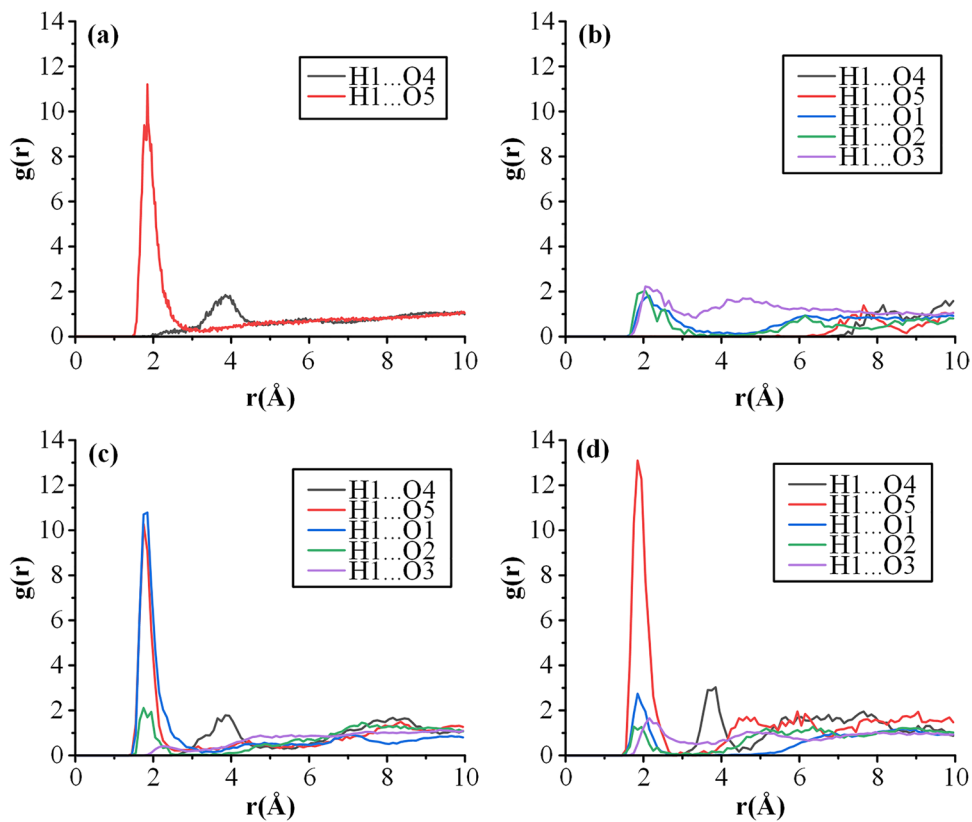

Fig. 8 Radial distribution functions, g(r), between SDR's -OH proton (H1) and **a** SDR's HB acceptor oxygens (O4 and O5); SOL's H-bond acceptor oxygens (O1 to O3) in SDR-SOL amorphous assemblies having 10/90% (**b**), 20/80% (**c**), and 30/70% (**d**) *w/w* of API to polymer ratio

amorphous phase, leading to the formation of three different/distinct zones: (1) neat amorphous SDR, (2) neat SOL, and (3) molecularly dispersed SDR within SOL. Finally, a further increase in the drug's content seems to favor the formation of neat amorphous SDR, which will eventually lead to phase separation between the amorphous SDR and matrix/carrier, and, consequently, to SDR's recrystallization.

Conclusion

Nowadays, there is an urgent need to discover new bioactive ingredients with improved antioxidant activity. This is especially important in the therapy of various diseases (such as periodontitis) where reactive oxygen species are involved in their pathogenesis. The use of natural products is one of the main strategies in this direction. However, despite their significant advantages (including anti-inflammatory and antioxidant properties), many of these active compounds do not present the preferable physiochemical properties so as to be successfully formulated into orally administrated pharmaceutical products. In this context, the present study has successfully managed to prepare for the first time an ASD formulation for the active ent-kaurane diterpenoid substance, SDR. According to the obtained results, SOL proved to be the most appropriate matrix/carrier for the preparation of SDR-based ASDs, probably due to its good miscibility with the API and the formation of strong intermolecular interactions (H-bonds) between them (revealed *via* both ATR-FTIR spectroscopy and MD simulations). The prepared ASDs were stable during storage, since no API crystals were observed after several months. Therefore, it can be concluded that the development of an ASD based on SOL seems to be a successful technique for the formulation of the poor water-soluble API SDR, although further studies are needed in order to advance these findings into a final marketed finished dosage form.

Declarations

Conflict of Interest The authors declare no competing interests.

References

1. Gong L-L, Du L-D, Du G-H. Theophylline. Natural small molecule drugs from plants: Springer; 2018. p. 469–74.
2. Jain H, Chella N. Solubility enhancement techniques for natural product delivery. Sustainable Agriculture Reviews 43: Springer; 2020, 33–66.
3. Tomou E-M, Chatziathanasiadou MV, Chatzopoulou P, Tzakos AG, Skaltsa H. NMR-based chemical profiling, isolation and evaluation of the cytotoxic potential of the diterpenoid siderol from cultivated Sideritis euboea Heldr. Molecules. 2020;25(10):2382.
4. Tadić V, Bojović D, Arsić I, Ðorđević S, Aksentijevic K, Stamenić M, et al. Chemical and antimicrobial evaluation of supercritical and conventional Sideritis scardica Griseb., Lamiaceae extracts. Molecules. 2012;17(3):2683–703.
5. Tadić VM, Jeremic I, Dobric S, Isakovic A, Markovic I, Trajkovic V, et al. Anti-inflammatory, gastroprotective, and cytotoxic effects of Sideritis scardica extracts. Planta Med. 2012;78(05):415–27.
6. Wightman EL, Jackson PA, Khan J, Forster J, Heiner F, Feistel B, et al. The acute and chronic cognitive and cerebral blood flow effects of a Sideritis scardica (Greek Mountain Tea) extract: a double blind, randomized, placebo controlled, parallel groups study in healthy humans. Nutrients. 2018;10(8). https://doi.org/10.3390/nu10080955.
7. González-Burgos E, Duarte AI, Carretero ME, Moreira PI, Gómez-Serranillos MP. Kaurane diterpenes as mitochondrial alterations preventive agents under experimental oxidative stress conditions. Pharm Biol. 2016;54(4):705–11.
8. Carikci S, Goren AC, Kilic T. Diterpenoid and phenolic contents of Sideritis hololeuca Boiss & Heldr. Apud Bentham with antioxidant and anticholinesterase activity. Zeitschrift für Naturforschung C. 2020;75(5–6):161–9. https://doi.org/10.1515/znc-2019-0161.
9. Sagir ZO, Carikci S, Kilic T, Goren AC. Metabolic profile and biological activity of Sideritis brevibracteata P. H. Davis endemic to Turkey. International Journal of Food Properties. 2017;20(12):2994–3005. https://doi.org/10.1080/10942912.2016.1265981.
10. Topçu G, Ertaş A, Öztürk M, Dinçel D, Kılıç T, Halfon B. Ent-kaurane diterpenoids isolated from Sideritis congesta. Phytochem Lett. 2011;4(4):436–9. https://doi.org/10.1016/j.phytol.2011.05.001.
11. Sczepanik FSC, Grossi ML, Casati M, Goldberg M, Glogauer M, Fine N, et al. Periodontitis is an inflammatory disease of oxidative stress: we should treat it that way. Periodontology 2000. 2020;84(1):45–68. https://doi.org/10.1111/prd.12342.
12. Da Silva FLO, Marques MBDF, Kato KC, Carneiro G. Nanonization techniques to overcome poor water-solubility with drugs. Expert Opin Drug Discov. 2020;15(7):853–64.

13. Williams RO III. Watts AB, Miller DA. Formulating poorly water soluble drugs: Springer; 2016.

14. Sridhar I, Doshi A, Joshi B, Wankhede V, Doshi J. Solid dispersions: an approach to enhance solubility of poorly water soluble drug. J Sci Innov Res. 2013;2(3):685–94.

15. Graeser KA, Patterson JE, Zeitler JA, Rades T. The role of configurational entropy in amorphous systems. Pharmaceutics. 2010;2(2):224–44.

16. Williams HD, Trevaskis NL, Charman SA, Shanker RM, Charman WN, Pouton CW, *et al*. Strategies to address low drug solubility in discovery and development. Pharmacol Rev. 2013;65(1):315–499. https://doi.org/10.1124/pr.112.005660.

17. Bhalodiya M, Chavda J, Mori D, Patel N, Manek R, Dudhat K. Formulation and evaluation of amorphous solid dispersion Boerhaavia diffusa methanolic root extract for improving dissolution properties. Journal of Drug Delivery Science and Technology. 2021;66: 102740.

18. Bharate SS. Enhancing biopharmaceutical attributes of Khellin by amorphous binary solid dispersions. AAPS PharmSciTech. 2021;22(8):1–14.

19. Jin S, Lee CH, Lim DY, Lee J, Park S-J, Song I-S, *et al*. Improved hygroscopicity and bioavailability of solid dispersion of red ginseng extract with silicon dioxide. Pharmaceutics. 2021;13(7):1022.

20. Lim C, Kang JK, Jung CE, Sim T, Her J, Kang K, *et al*. Preparation and characterization of a lutein solid dispersion to improve its solubility and stability. AAPS PharmSciTech. 2021;22(5):1–9.

21. Tong M, Wu X, Zhang S, Hua D, Li S, Yu X, *et al*. Application of TPGS as an efflux inhibitor and a plasticizer in baicalein solid dispersion. Eur J Pharm Sci. 2022;168: 106071.

22. Baird JA, Van Eerdenbrugh B, Taylor LS. A classification system to assess the crystallization tendency of organic molecules from undercooled melts. J Pharm Sci. 2010;99(9):3787–806.

23. Kapourani A, Tzakri T, Valkanioti V, Kontogiannopoulos KN, Barmpalexis P. Drug crystal growth in ternary amorphous solid dispersions: effect of surfactants and polymeric matrix-carriers. International journal of pharmaceutics: X. 2021;3: 100086.

24. Mosquera-Giraldo LI, Trasi NS, Taylor LS. Impact of surfactants on the crystal growth of amorphous celecoxib. Int J Pharm. 2014;461(1–2):251–7.

25. Djuris J, Nikolakakis I, Ibric S, Djuric Z, Kachrimanis K. Preparation of carbamazepine–Soluplus® solid dispersions by hot-melt extrusion, and prediction of drug–polymer miscibility by thermodynamic model fitting. Eur J Pharm Biopharm. 2013;84(1):228–37.

26. Marsac PJ, Shamblin SL, Taylor LS. Theoretical and practical approaches for prediction of drug–polymer miscibility and solubility. Pharm Res. 2006;23(10):2417–26.

27. Hoftyzer PJ, Van Krevelen DW. Properties of polymers. 2nd ed. New York: Elsevier; 1976.

28. Breitkreutz J. Prediction of intestinal drug absorption properties by three-dimensional solubility parameters. Pharm Res. 1998;15(9):1370–5.

29. Greenhalgh DJ, Williams AC, Timmins P, York P. Solubility parameters as predictors of miscibility in solid dispersions. J Pharm Sci. 1999;88(11):1182–90.

30. Gómez-Serranillos MP, El-Naggar T, Villar AM, Carretero ME. Analysis and retention behaviour in high-performance liquid chromatography of terpenic plant constituents (Sideritis spp.) with pharmacological interest. Journal of Chromatography B. 2004;812(1):379–83. https://doi.org/10.1016/j.jchromb.2004.09.050.

31. Barmpalexis P, Karagianni A, Kachrimanis K. Molecular simulations for amorphous drug formulation: polymeric matrix properties relevant to hot-melt extrusion. Eur J Pharm Sci. 2018;119:259–67. https://doi.org/10.1016/j.ejps.2018.04.035.

32. Kapourani A, Eleftheriadou K, Kontogiannopoulos KN, Barmpalexis P. Evaluation of rivaroxaban amorphous solid dispersions physical stability via molecular mobility studies and molecular simulations. Eur J Pharm Sci. 2021;157: 105642. https://doi.org/10.1016/j.ejps.2020.105642.

33. Azizoglu A, Özer Z, Kiliç T. An experimental and theoretical study on siderol isolated from Sideritis species. Collect Czech Chem Commun. 2011;76:95–114. https://doi.org/10.1135/cccc2010119.

34. Li D, Panchal K, Mafi R, Xi L. An atomistic evaluation of the compatibility and plasticization efficacy of phthalates in poly(vinyl chloride). Macromolecules. 2018;51(18):6997–7012. https://doi.org/10.1021/acs.macromol.8b00756.

35. Gunsteren WFv, Mark AE. Validation of molecular dynamics simulation. The Journal of Chemical Physics. 1998;108(15):6109–16. https://doi.org/10.1063/1.476021.

36. Tian B, Tang X, Taylor LS. Investigating the correlation between miscibility and physical stability of amorphous solid dispersions using fluorescence-based techniques. Mol Pharm. 2016;13(11):3988–4000.

37. Newman A, Engers D, Bates S, Ivanisevic I, Kelly RC, Zografi G. Characterization of amorphous API: polymer mixtures using X-ray powder diffraction. J Pharm Sci. 2008;97(11):4840–56.

38. Yuan X, Sperger D, Munson EJ. Investigating miscibility and molecular mobility of nifedipine-PVP amorphous solid dispersions using solid-state NMR spectroscopy. Mol Pharm. 2014;11(1):329–37.

39. Anane-Adjei AB, Jacobs E, Nash SC, Askin S, Soundararajan R, Kyobula M, *et al*. Amorphous solid dispersions: utilization and challenges in preclinical drug development within AstraZeneca. Int J Pharm. 2022;614: 121387. https://doi.org/10.1016/j.ijpharm.2021.121387.